AIAA JOURNAL
Vol. 48, No. 11, November 2010

Experimental and Computational Study of Nonreacting Vortex Breakdown in a Swirl-Stabilized Combustor

Chukwueloka O. U. Umeh*
General Electric Aviation, Cincinnati, Ohio 45215
Zvi Rusak†
Rensselaer Polytechnic Institute, Troy, New York 12180-3590
Ephraim Gutmark‡ and Rodrigo Villalva§
University of Cincinnati, Cincinnati, Ohio 45221
and
Dong-Jin Cha¶
Hanbat National University, Daejeon 305-719, Republic of Korea

DOI: 10.2514/1.J050393

Nonreacting flow experiments are conducted in a swirl-stabilized combustor with several configurations of a triple annular research swirler fuel injector. Particle imaging velocimetry is used to measure mean axial, radial, and tangential distribution of the velocity field, from which the swirl ratio and the position of vortex breakdown are calculated for each injector configuration. Numerical simulations based on the Reynolds-averaged Navier–Stokes model equations of nonreacting flows provide insight into the characteristics of the axisymmetric vortex breakdown phenomenon in a circular, finite-length pipe with a sudden expansion downstream of a concentric, circular inlet pipe. Results show that flow states with vortex breakdown can be simulated numerically. Good agreement is found between the results of the simulations and available theoretical predictions for the first appearance of breakdown downstream of the pipe expansion plane, as well as its first appearance in the inlet pipe section as the inlet swirl level is increased. Good agreement is also shown between the measured experimental data, simulations, and theoretical predictions. It is demonstrated that the theoretical criteria and numerical simulations can be used to predict the appearance and location of vortex breakdown for several different nozzles of varying swirl numbers relevant to the stability of lean, premixed combustion.

I. Introduction

IN THE recent past, stationary gas turbine engine combustors typically operated on turbulent diffusion flames due to the relative stability of the diffusion combustion process. A consequence of this process, however, is the generation of high levels of NOx (about 200 ppm on a dry, 15% O_2 basis) [1] due to relatively poor fuel–air mixing. Within the past two decades, gas turbine combustors now rely more on lean premixed (or partially premixed) flames to meet increasingly stringent emissions regulations. In lean premixed (LPM) combustion systems, most of the fuel and air are mixed before combustion, thereby reducing the likelihood of localized stoichiometric regions in the reaction zone. The main advantage of this system is that the equivalence ratio in the main reaction zone is lean, thereby drastically reducing the production of NOx compared with diffusion combustors of comparable power output. The major drawback of LPM systems is their susceptibility to pressure fluctuations (generally referred to as combustion dynamics), autoignition, flashback, and lean blowout [1].

In many ground-based LPM combustors, flame stabilization is achieved with the use of upstream swirl and a sudden expansion at the dump plane (the inlet plane to the combustion chamber). In many of these combustors, swirl is introduced to the incoming fuel–air mixture by stationary swirl vanes, which creates a vortex flow in the axial direction [2]. The sudden expansion at the backward-facing step forces a sudden increase in the diameter of the tight, coherent vortex line and a decrease in axial velocity in the vortex core. If the swirl is high enough, the vortex breaks down in the combustion chamber, often forming a center recirculation zone (CTRZ) and corner recirculation zones (CRZ) near the dump plane. These recirculation zones entrain unreacted fuel–air from the incoming flow and stabilize the compact premixed flame.

With a properly optimized swirler, the premixed flame is located just aft of the dump plane. The flame is compact, permitting the design of a shorter, lighter combustor in comparison with a diffusion flame-stabilized combustor. If the inlet swirl level is too low, the CTRZ is not present and the CRZs are too weak to anchor the flame, which blows out. On the other hand, if the swirl level is too high, the CTRZ moves upstream into the injection region and may cause flashback. Thermoacoustic instabilities (dynamics) can also be driven by the oscillation of the recirculation zones, causing noise and structural vibrations within and around the combustor [3–6].

Grinstein et al. [7] performed three-dimensional (3-D) numerical studies of nonreacting swirling flows in an axisymmetric swirl-stabilized combustor with an expansion downstream of an inlet pipe. Using inlet conditions such as that of the General Electric (GE) LM6000 gas turbine, the formation of a center toroidal recirculation zone around the jet axis was observed for 1 atm, 300 K, and 4% pressure drop across the swirler inlet. Experiments confirmed that this quasi-axisymmetric CTRZ is developed by the vortex breakdown (VB) process.

Konle et al. [8] concluded from numerical simulations and experiments that, with increasing inlet mass flow, the upstream propagation due to combustion-induced vortex breakdown (CIVB) occurs at

---

Presented as Paper 2009-0643 at the 47th AIAA Aerospace Sciences Meeting, Orlando, FL, 5–8 January 2009; received 18 December 2009; revision received 10 June 2010; accepted for publication 11 June 2010.

[*] Engineering Manager, Commercial and Military Engines CDN Module, Product Engineering Center.

[†] Professor, Department of Mechanical, Aerospace, and Nuclear Engineering. Associate Fellow AIAA.

[‡] Distinguished Professor of Aerospace Engineering and Engineering Mechanics, Ohio Regents Eminent Scholar.

[§] Doctoral Candidate. Student Member AIAA.

[¶] Professor, Department of Building Services Engineering.

higher equivalence ratios in a swirl-stabilized combustor. They noted that higher inlet swirl levels induce stronger VB and that for the higher swirl levels, CIVB occurs at lower equivalence ratios due to the weaker flow stability.

The mechanism of vortex (swirl) generation by devices such as swirlers is due to strong viscous effects. However, once the vortex flow is generated, the mechanism that leads to VB in high-Reynolds-number flows is supposedly related largely to inviscid (dynamical) effects [9–16]. Until recently, the relationship between various theoretical and numerical solutions had not been fully clarified, nor were unambiguous criteria given for the occurrence, stability, and dynamics of VB.

Recently, a novel theoretical framework has been developed for predicting the axisymmetric VB process [10,17–25]. The approach, employing the Euler and Navier–Stokes formulations, examined the dynamics of axisymmetric swirling flows in a cylindrical chamber of finite length. The results, established through rigorous, nonlinear, global analysis, provide a fundamental and nearly complete mathematical description of the dynamics and stability of nonreacting, axisymmetric, swirling flows. The results show goodcorrelation with numerical computations and experimental studies [20–22]. This theory unifies in a natural way the major previous theoretical and numerical approaches to axisymmetric VB, fills the void between the various theories, and provides a global understanding of the process.

In this paper, we compare results of numerical simulations, analytical predictions, and particle imaging velocimetry (PIV)-measured data from experiments of nonreacting flows in a chamber with a circular inlet section and a sudden pipe expansion. The numerical studies are described in Sec. II, experimental work is discussed in Sec. III, and results of the experiments are compared with theoretical predictions and numerical calculations in Sec. IV.

For clarity, the basic study and test conditions are summarized as follows: for all the computational studies, inlet flow was characterized by temperature, pressure, and axial velocity w of 300 K, 1 atm, and 104 m/s, respectively, and the chamber expansion ratio was 3.0. The inlet swirl ratio at the mixing tube entrance was varied from 0 to 1.9. For the experiments, the inlet variables were air temperature $T3 = 300$ K, pressure $P3 = 1.02$ atm, and airflow rates $Wa = 30$ and 50 g/s, and chamber expansion ratio was 2.25. The inlet swirl ratio at the mixing tube entrance was varied from 0.59 to 1.35 by using various swirlers, as described in Sec. III. All these cases are characterized by low-Mach-number and high-Reynolds-number flows. The works of [9,19,25] show that the effects of compressibility and slight viscosity in such flows on the first appearance of VB and the size of the breakdown zone is negligible. The difference in expansion ratio between computations and experiments also has only a slight effect on the first appearance of breakdown [21,23].

II. Numerical Studies

A. Numerical Scheme

Numerical simulations based on the Reynolds-averaged Navier–Stokes (RANS) model equations of turbulent, nonreacting flows are performed using FLUENT version 6.2.16. For practical purposes, the geometry used for this analysis is derived from a single-cup combustor sector of a GE aeroderivative gas turbine engine (Fig. 1) scaled from the LM6000 gas turbine combustor, including its premixing fuel injector. The injector shown introduces a fixed swirl level to incoming airflow via static vanes oriented at a prespecified angle within its annulus.

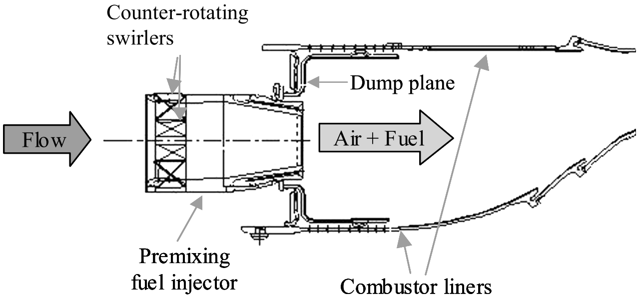

Fig. 1 Aeroderivative single-nozzle combustor sector with premixing fuel injector.

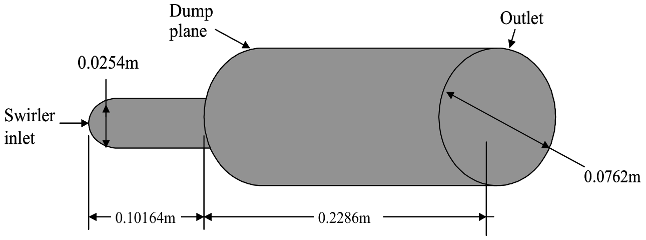

Fig. 2 A simplified combustor model.

As earlier mentioned, one of the main features that is observed in swirling flows in a dump combustor is the formation of a quasi-axisymmetric center toroidal recirculation zone around the axis of the jet. With this expected axisymmetric behavior, the combustor geometry shown in Fig. 1 is simplified to a model chamber of symmetric, cylindrical geometry, shown in Fig. 2. For modeling accuracy, we maintain the geometric scale between the sector of Fig. 1 and the simplified model of Fig. 2 within 95%. The important dimensions considered are the premixing section axial length and diameter, the chamber expansion ratio, and the hydraulic diameter of the chamber volume. The sudden expansion ratio is $R/R_i = 3$ (here, R_i is the inlet section radius, and R is the dump region radius). With the assumption of axisymmetric flow in the combustor, the domain is discretized with a numerical grid. An example is shown in Fig. 3. Reference [26] gives more details on the modeling.

The coupled, implicit solver of FLUENT in its compressible and axisymmetric formulation is used, since it solves the continuity, momentum, and energy equations simultaneously. This solver is suited to handling compressible flows with rotational forces or swirl [27]. The transport equations are solved in the unsteady, laminar, or turbulent modes, depending on the inlet Reynolds number. The first-order implicit unsteady formulation and the realizable k-epsilon model with standard wall functions are used to include turbulence effects in the flow. This model has been extensively validated for a wide range of flows, including rotating homogeneous shear flows, jets, mixing layers, boundary-layer flows, and wall-separated flows. It also correctly predicts the spreading rate for axisymmetric jets. In all computations, the turbulence viscosity ratio of 10 was used. The main weakness of using the k-epsilon model in our computations is that the turbulence levels inside the breakdown zone, and specifically around the leading edge of the zone, are not accurately predicted.

The inlet swirling flow at the beginning of the premixing inlet section is modeled by a solid-body rotation profile with a uniform axial speed w and rotation rate $\dot{\theta}$. The inlet swirl ratio is defined as $\Omega = \dot{\theta}R_i/w$. This ratio Ω represents the swirl number of the swirler ahead of the inlet section (i.e., at the swirler exit plane) that generates the inlet rotating flow. In all the present simulations, the inlet flow is also characterized by temperature, pressure, and axial velocity w of 300 K, 1 atm, and 104 m/s, respectively. The pressure outlet boundary condition is used, since it is assumed that the flow exhausts to ambient pressure. The no-slip and no-penetration conditions are imposed along the chamber walls, and flow symmetry conditions are used along the centerline.

To model transient phenomena properly, it is necessary to set the computational time step for each iteration at least one order of magnitude smaller than the smallest time scale characterizing the

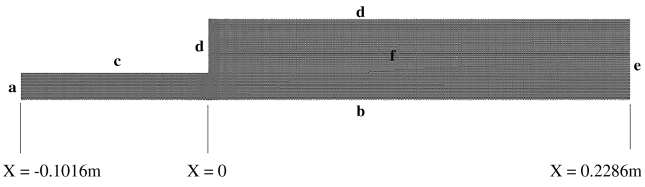

Fig. 3 Computational domain with 27,210 elements (26,308 cells).

case under consideration. In the present study, the smallest time scale was obtained from the characteristic flow time in rotation, $R_i/V_t = 1/\dot{\theta}$, where R_i, V_t, and $\dot{\theta}$ are the inlet radius (m), inlet tangential velocity (m/s), and inlet angular velocity (rad/s), respectively.

The effects of mesh refinement on the solution were investigated [26,28] using three uniform meshes consisting of 15,238 cells, 26,308 cells, and 40,198 cells. Each case was run until the solution reached a near-time-asymptotic behavior along the inlet section and in front of the breakdown zone, i.e., until there was a change less than 0.01 m/s in the axial velocity upstream of a selected axial location downstream of the dump plane. The mesh refinement studies showed that the mesh with 26,308 cells yields solutions of equal accuracy with the finer mesh but in less computational time. It was therefore used for all the numerical simulations.

The effects of varying the inlet swirl ratio Ω on the stability of the flow and the appearance of breakdown states in the dump region and inside the premixing inlet section are investigated. Results are shown in Sec. II.C.

B. Theoretical Prediction of Vortex Breakdown

The VB process was analyzed and explained by the work of Rusak and Wang [16], Wang and Rusak [17–19], Malkiel et al. [20], Rusak et al. [21,22], Judd et al. [23], Rusak [24], and Rusak and Lee [25]. According to [16–21], two critical swirl ratios, ω_0 and ω_1, exist for a confined swirling flow in a straight pipe, where $\omega_0 < \omega_1$. For the case with $\omega < \omega_0$, a nearly columnar flow state prevails throughout the pipe length and is a unique solution of the unsteady and axisymmetric Navier–Stokes equations. Two stable steady-state solutions coexist in the range of incoming swirl $\omega_0 < \omega < \omega_1$: a local minimizer solution describing a columnar swirling flow and a global minimizer solution describing a swirling flow with a large stagnation breakdown region. An unstable branch of min–max solutions connects these two solution branches. The solution that manifests itself depends on the initial disturbances introduced to the base columnar flow; that is, small perturbations decay in time, and the columnar state prevails, while large disturbances enforce a transition (the breakdown process) to the breakdown state. When $\omega > \omega_1$, the columnar swirling flow is unstable, and the flow always transitions to a VB state. Therefore, $\omega > \omega_0$ is a necessary condition for breakdown, and $\omega > \omega_1$ is a sufficient condition. It is expected that in a turbulent flow in a noisy environment (i.e., an environment with flow disturbances), the flow will transition to breakdown when $\omega > \omega_0$. In addition, in an expanding chamber, breakdown will move into the inlet section when $\omega > \omega_1$. It is therefore expected that a stable VB occurs within the chamber dump region in the range of $\omega_0 \leq \omega \leq \omega_1$. It should be noted here that Rusak et al. [22] applied their mathematical theory of VB to predict the values of swirl ratio, ω_0 and ω_1, for a Q-vortex flow model. Keller et al. [29] results can be used to compute ω_0 and ω_1 using a Rankine vortex flow model, specifically with a large vortical core radius r_c.

In the present study, we are specifically interested in the flow states slightly downstream of the dump plane (i.e., at $x = 0$) and at the exit of the swirler (the beginning of the premixing inlet section at $x = -0.1016$ m). Slightly downstream of the dump plane and before breakdown occurs, the flow is characterized by a strong swirling jet and may be represented by the Q-vortex flow model with a strong jet (jet parameter $\delta > 1$) and a core radius ratio $r_c/R_i = 0.3$ (slightly smaller than the inverse of the sudden expansion ratio of the chamber). At the exit of the swirler and the beginning of the premixing inlet section, the flow may be represented by a Rankine vortex with a large vortical core radius ratio, $r_c/R_i = 0.96$, and with a uniform axial speed (a near solid-body rotation flow profile). The swirl ratio of the near-solid-body rotation at this section is also the swirl number of the inlet flow Ω. Using the works of Rusak et al. [22] and Keller et al. [29], the critical swirl levels for these two vortex flow profiles can be computed. A summary of the results is given in Table 1. Here, the critical swirl ratios are given by $\omega_0 = Vt_{\max}/Vz_0|_0$ and $\omega_1 = Vt_{\max}/Vz_0|_1$, where $Vt_{\max}$ is the maximum circumferential velocity at a certain cross section, and Vz_0 is the centerline axial velocity at that cross section. These theoretical calculations predict that VB appears in the inert swirling flow in the dump region only when the velocity profile slightly downstream of the dump plane exceeds a critical ratio, $Vt_{\max}/Vz_0 = 0.67$. Also, it is predicted that the breakdown zone will penetrate into the premixing inlet section when the swirl number $\Omega > 1.87$.

Table 1 Breakdown criteria based on Rusak et al.'s Q-vortex model [22] and Keller et al.'s Rankine vortex model [29]

VB Position	r_x/r_t	$\omega_0 = V_{\max}/w\|_0$	$\omega_1 = V_{\max}/w\|_1$
Breakdown criteria based on Rusak et al.'s Q-vortex model [22]			
Dump region	0.3	0.67	0.90
Breakdown criteria based on Keller et al.'s Rankine vortex model [29]			
Inlet region	0.96	1.87	1.90

C. Numerical Results

The inert flowfield within the model chamber was computed for various levels of the inlet swirl ratio (swirl number Ω in the range between 0 and 2.0). Figures 4 and 5 show the computed axial velocity fields at various Ω from the RANS simulations. These figures show a gradual transition to a VB state in the dump region as Ω is increased. A stagnation point along the centerline and a VB zone (CTRZ) first appear at $\Omega = 0.88$. Computations also show the movement of the CTRZ as Ω is further increased. When $\Omega > 1.84$, the breakdown point and the CTRZ penetrate into the inlet region.

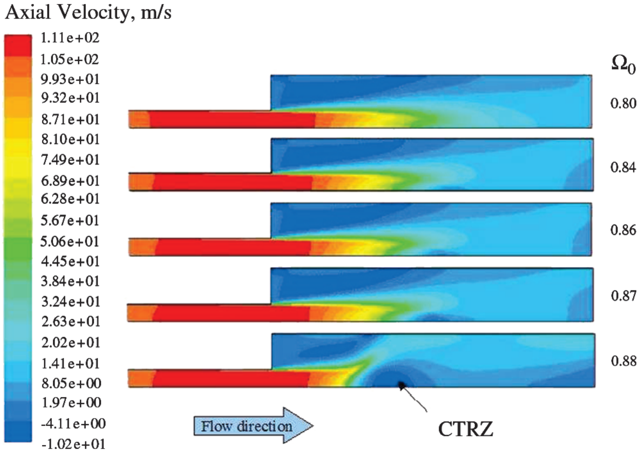

Fig. 4 Contours of axial velocity showing the first appearance of a VB state in the dump region for different Ω.

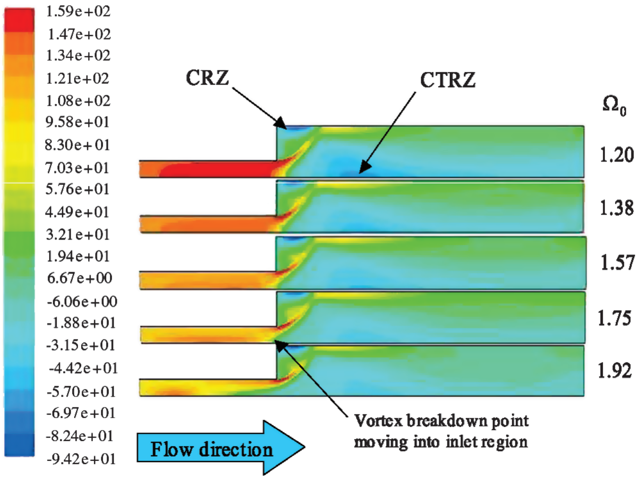

Fig. 5 Contours of axial velocity showing the transition toward the first appearance of a VB state in the inlet region.

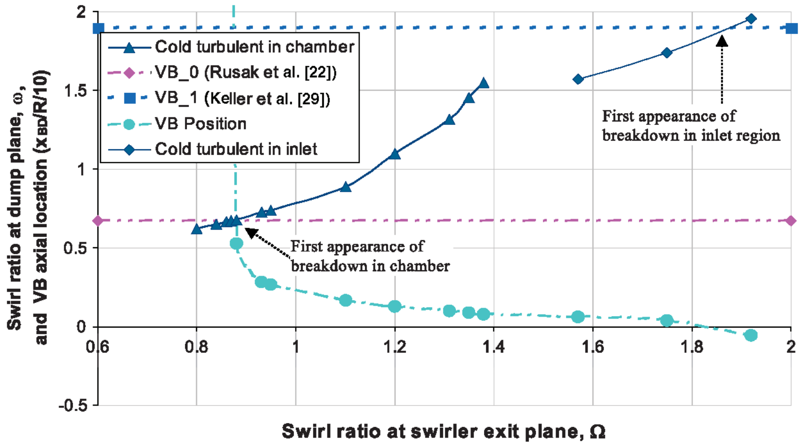

Fig. 6 Swirl ratio at dump plane and normalized axial position of VB vs inlet swirl ratio. Comparison of analytical VB criteria by Rusak et al. [22] and Keller et al. [29] with numerical results.

The RANS computations provide the position of the breakdown (stagnation) point x_{BD} as a function of the inlet swirl ratio Ω. This is shown in Fig. 6 by the light blue dashed–dotted line connecting solid light blue circles. For this plot, the horizontal axis is the swirl ratio (swirl number) at the swirler inlet Ω, while the vertical axis is the normalized breakdown location divided by $10(x_{\mathrm{BD}})/R)/10$. Also shown in Fig. 6 are the computed swirl ratio, $\omega = Vt_{\max}/Vz_0$, at the dump plane (the solid blue line connecting solid blue triangles) and the computed swirl ratio, $\omega = \Omega$, of the flow at the inlet of the mixing inlet section (for $\Omega > 1.56$). In addition, the theoretically predicted critical values of $\omega = Vt_{\max}/Vz_0 = 0.67$ (the horizontal purple dashed–double-dot line) and of $\omega = 1.87$ (the horizontal blue dashed line) are shown. The figure shows that, indeed, when the swirl ratio $\omega = Vt_{\max}/Vz_0$ at the dump plane exceeds the critical level, 0.67, VB first appears in the dump region. This corresponds to a swirl number, $\Omega = 0.88$, at the inlet of the mixing section. The swirl ratio, $\omega = Vt_{\max}/Vz_0$, at the dump plane increases significantly and tends to infinity as the swirl number Ω is further increased, the breakdown point and zone move upstream, and the axial speed at the dump plane is significantly decreased. Also, when the swirl number Ω exceeds the critical level of 1.84, the breakdown point moves into the inlet section, and this correlates well with the theoretically predicted critical value of 1.87.

III. Experimental Studies

A. Experimental Setup

The test setup is an atmospheric combustor, which comprises a flow-conditioning inlet chamber with four flow screens inserted at its upstream end, an air inlet plenum, a 48-mm-long 51-mm-diam mixing tube mounted at the downstream end of the inlet plenum, and a $110 \times 110 \times 480$ mm combustion chamber mounted vertically on the mixing tube flange (Fig. 7). The inlet chamber and inlet plenum are made of 152 mm (4 in.) diameter steel pipes, while the combustion chamber is made of clear polycarbonate sheets. The exit plane of the mixing tube is coplanar with the dump plane and expands directly into the combustion chamber. Air is supplied to the inlet plenum from a blowdown chamber via a pressure-regulating valve and a 36 kw electric heater. The fuel injector is a triple annular research swirler (TARS) developed by Delavan Gas Turbine Products, a division of Goodrich Corporation, in collaboration with GE Aviation. The injector is installed in the inlet plenum, with its exit inserted snugly into the upstream end of the mixing tube. All the air delivered to the inlet plenum enters the combustion chamber through the fuel nozzle. The TARS comprises radial outer, axial intermediate, and axial inner swirl vanes arranged concentrically to the longitudinal axis. The angle of each swirler annulus can be changed

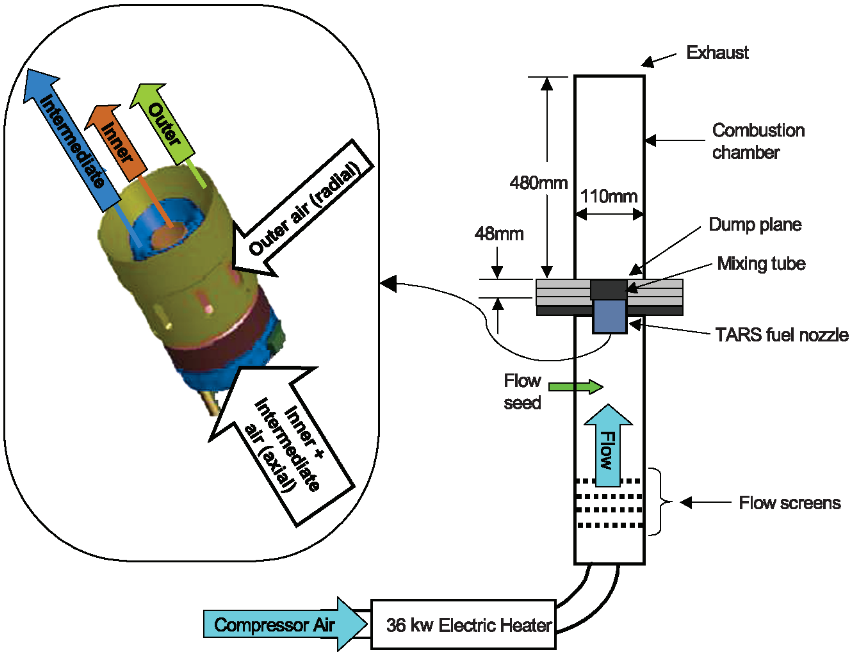

Fig. 7 Test setup for nonreacting flow experiments.

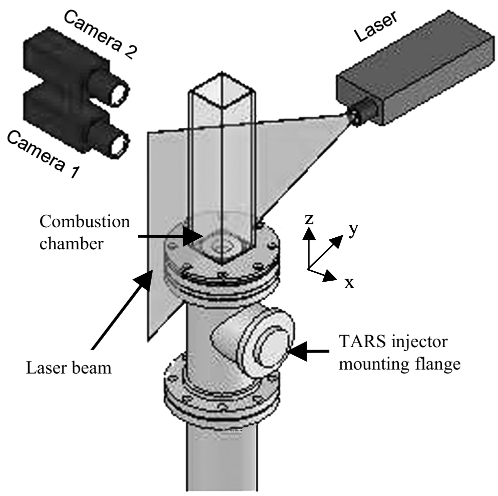

Fig. 8 2-D axial PIV setup.

independent of the other two, resulting in over 30 possible discrete geometric swirl numbers with the available hardware. Each arrangement of available swirlers is referred to as a configuration in this work and is denoted with six digits. An example is 300045, which refers to a configuration with the outer swirler vanes at 30° to the radial axis, the intermediate swirler vanes at 0° to the axial, and the inner swirler vanes at 45° to the axial plane. Individual swirlers impart a clockwise swirl to the flow (aft looking downstream). A counterclockwise swirler is prefixed with “n”; for example, n303030_35 refers to -30° outer, 30° intermediate, and 30° inner swirler. The “_35” suffix refers to an airflow rate of 35 grams per second for this particular test. See [30] for more details on the TARS. Measurements made in these tests are inlet air mass flow rate, temperature, and pressure, each with an accuracy of 1%, $+1.1^\circ$C, and $+0.04$ psig, respectively.

Figures 8 and 9 show two separate PIV setups used for axial two-dimensional (2-D) and radial 3-D (stereoscopic) PIV imaging of the confined flowfield within the combustion chamber shown. The combustor flows imaged are nonreacting, and they are at ambient temperature and pressure. A double-pulsed neodymium-doped yttrium aluminum garnet laser (New Wave, Solo PIV) with pulse energy of up to 120 mJ per pulse at 15 Hz and a wavelength of 532 nm provides a 1-mm-thick laser sheet used for planar illumination. In the 2-D setup, two 12-bit Powerview charge-coupled device cameras, model 630049, are set up on the same side of the combustor chamber, perpendicular to the illuminated plane. The laser sheet bisects the combustor axially from the dump plane to the exit plane and is set at 10 μs between pulses. Camera 1 images from the dump plane to 140 mm, and camera 2 continues from 141 to 280 mm along the combustor axis. The 2-D tests yield the Vx (axial) and Vy (radial) velocity components.

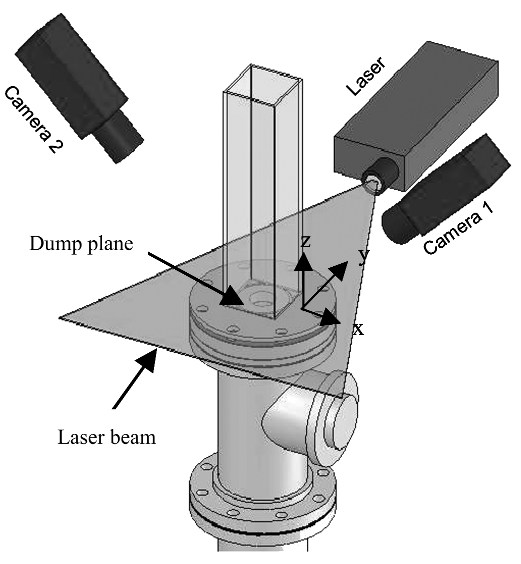

Fig. 9 3-D radial PIV setup.

For the 3-D tests, the laser sheet is perpendicular to the flow and is positioned 6.35 mm downstream of the combustor dump plane to avoid reflections from the dump plate. Cameras 1 and 2 are set on opposite sides of the chamber, looking down at the illuminated plane at an angle to the vertical axis. From this test, we get the Vx (radial), Vy (radial), and Vz (axial) components of velocity. Tangential (circumferential) velocity Vt is then computed from x and y coordinates and Vx and Vy velocity components. In both 2-D and 3-D tests, 250 images are taken for each configuration and post-processed to yield the velocity components, kinetic energy, turbulent kinetic energy, and turbulent shear.

Olive oil mist used for seeding is supplied to the inlet plenum with a four-hole pressure chamber atomizer upstream of the swirler inlet, providing particles in the size range of 1–3 μm. Based on this particle diameter, lag error due to the difference in density of the fluid and seeding particles can be computed using Stokes’ law. The lag error is proportional to the square of the particle diameter and to the acceleration experienced by the particle. For the current study, this involves gravitational acceleration and convective acceleration within the flow. Assuming the largest particle size, the velocity error due to gravity acceleration is $2.60\text{E}-04\ \text{m/s}$. Convective acceleration is more difficult to quantify, since change in velocity along particle trajectories is necessary. However, because there are no shock waves in the flow and no sudden expansion across a flame front, lag error is expected to be low, since the spatial velocity derivative never approaches a step change. Even if convective acceleration were to be three orders of magnitude higher than gravity acceleration, lag error would remain at less than $1\ \text{m/s}$ at the regions of the strongest gradients. Thus, the main errors in PIV measurements are mainly due to nonuniformity and density of flow seeding, reflection of laser light from the combustor chamber walls, reduction in optical access due to windows being obscured with seed, and errors due to pretest system calibration and posttest data processing. As a result, error in the 2-D and 3-D velocity data is difficult to estimate. Based on the observed variation in the 2-D and 3-D PIV data, the error bands for the nondimensional VB location, the swirl ratio at the dump plane, and the inlet swirl ratio are 0.03, 0.18, and 0.02, respectively. Furthermore, uncertainty in average velocity for turbulence of less than 5% is 1%.

Image processing was performed using multiple-pass post-processing with an initial window size of 64×64 pixels down to a final window size of 32×32 pixels, with a 50% overlap in each direction. As a result, this approach led to a measurement grid with a spatial resolution of about 1.5×1.5 mm for the 2-D measurements, with the resolution of the 3-D images being in the same range. Smoothing of the data was performed only after vector calculations were completed. A time interval of 10 μs between laser pulses was used.

It should be noted here that, in the experimental apparatus, the sudden expansion ratio based on the mixing tube radius and chamber hydraulic diameter is $R/R_i \approx 2.25$ and is slightly lower than that in the numerical computations. Therefore, the predicted critical swirl for the first appearance of VB in the dump region is based here on a vortex core radius ratio of $r_c/R = 0.4$ at the dump plane and is slightly increased. Then, from Rusak et al. [21], we find that the critical ratio $Vt_{\max}/Vz_0 = 0.75$: i.e., in the experimental apparatus, it is expected that breakdown will first appear in the dump region when $\omega = Vt_{\max}/Vz_0 > 0.75$. The condition for the first appearance of breakdown in the inlet section is not affected by the expansion ratio and therefore does not change $\Omega > 1.87$.

Note also that a square chamber was used for the experiments instead of an axisymmetric chamber similar to that used for the computations to avoid the light-scattering effects encountered by using a cylindrical chamber in the PIV measurements. Since the computational simulations were carried out on an axisymmetric geometry, we do not have insight to the effect of wall corners on the observed breakdown phenomena. The use of a square chamber may not appreciably affect the experimental results since each of the internal corners of the square geometry was removed by the addition of a corner wedge, which helps to minimize the corner effects. Since the main aspect of the study, breakdown, and its location is thought to be mainly due to the dynamics of the CTRZ and the CRZs, the difference in the two geometries may not have an impact on the validity of the present work.

B. Data Analysis

In accordance with established convention, each swirler configuration is characterized by a swirl number or swirl ratio. A well-known method of calculating the swirl number S_N is based on momentum of flux through the swirler:

$$S_N = \frac{G_\varphi}{G_x R} \tag{1}$$

where

$$G_\varphi = \int_0^R (V_t r)\rho V_z 2\pi r \,\mathrm{d}r$$

$$G_x = \int_0^R \rho V_z^2 2\pi r \,\mathrm{d}r$$

and V_z and V_t are the axial and tangential components of the velocity, respectively, R is the radius of the cross-sectional plane, and r is the radial coordinate. Note that, for a solid-body rotation with a swirl ratio Ω and a uniform axial speed, $V_t = \Omega w r/R_i$, $V_z = \mathrm{const} = w$, and

$$S_N = \frac{\int_0^R (V_t V_z r^2)\,\mathrm{d}r}{R\int_0^R (V_z^2 r)\,\mathrm{d}r} = \frac{\int_0^R (\Omega w^2 \frac{r}{R} r^2)\,\mathrm{d}r}{R\int_0^R (w^2 r)\,\mathrm{d}r} = \frac{\Omega}{2} \tag{2}$$

or

$$\Omega = 2S_N$$

That is, the solid-body swirl ratio is twice the classical swirl number.

In our analytical and numerical work summarized in preceding sections, we characterized the different swirlers with the swirl ratio Ω of a solid-body rotation at the swirler exit plane, the beginning of the inlet section. Since we cannot measure the flow inside the mixing tube in the experiments, Ω cannot be measured directly. We therefore developed a method to compute Ω from the velocity measurements at the laser plane in Fig. 9. It is based on the relationship between the circulation function $K(r)$ and the volumetric reduced-flux function $Q(r)$:

$$K(r) = rV_t(r) \tag{3}$$

and

$$Q(r) = \int_0^r V_z(r')r'\,\mathrm{d}r'$$

Note that $K(r)$ is calculated based on the tangential velocity profile V_t, while Q is calculated from the axial velocity profile, $V_z(r)$. For a solid-body rotation flow downstream of the swirler exit plane, $V_t = \Omega w r/R_i$ and $V_z = \mathrm{const} = w$. Then,

$$Q(r) = \frac{wr^2}{2} \tag{4}$$

and

$$K = V_t r = \frac{\Omega w r^2}{R_i} = \frac{2\Omega Q}{R_i} \tag{5}$$

We find that a solid-body rotation flow is characterized by the fact that K is linearly proportional to Q; that is, a plot of K vs Q yields a linear line, and the slope of the line is $K/Q = 2\Omega/R_i$. The circulation and flux functions are conserved quantities of the swirling flow. Therefore, when the PIV-measured profiles of the axial and tangential speeds in the laser plane result in an approximately linear line of K vs Q within the area directly influenced by the swirler flow, it demonstrates that the assumption of a solid-body rotation of the upstream flow at the swirler exit plane is valid. The slope of this linear line K/Q is then used to compute the swirl ratio Ω at the swirler exit plane. That is,

$$\Omega = (K/Q)(R_i/2) \tag{6}$$

It should be noted that, in some of the data cases, the K vs Q plot shows a very nice linear behavior, in which case the slope is easily calculated. In a few other cases, where VB penetrates into the mixing inlet section, the data are somewhat noisy, possibly due to fluctuation of the precessing vortex, and the slope becomes somewhat more difficult to calculate. In addition, if the swirler is divided into two halves, Q and K on both sides should ideally be symmetric. However, the physics of the unsteady or asymmetric flow in the chamber tend to shift the plane of symmetry to either side, requiring a symmetrization of the data about the centerline before calculating the line slope and the swirl ratio.

Another swirl ratio of interest is ω, computed at the dump plane. This can be computed directly from the PIV-measured profiles of the axial and tangential speeds at a cross section immediately downstream of the dump plane:

$$\omega = V_{t\,\mathrm{max}}/V_{z0} \tag{7}$$

Vt_{max} is the maximum circumferential velocity at the cross section, and Vz_0 is the centerline axial velocity at that cross section.

2-D PIV axial images provide information on the presence and axial location of VB along the combustor centerline. Axial velocity is nondimensionalized with calculated swirler bulk exit velocity V, while axial location is nondimensionalized with the swirler exit radius. Since all the metered air delivered to the inlet plenum goes through the fuel nozzle, we can calculate the velocity V as $V = Wa/\rho A$, where Wa is the airflow mass rate, ρ is air density at the given flow conditions, and A is the swirler exit area. For each configuration, a plot of normalized axial velocity vs normalized centerline location is shown. A contour plot of axial velocity in the centerline plane is also generated for each swirler configuration to show a qualitative and quantitative picture of the flowfield.

From the 3-D PIV radial data, we calculate Q, K, ω, and Ω for each swirler configuration. For illustration, it is worthwhile to show the analysis conducted for two representative swirler configurations: namely, n303030, which exhibits no VB in the flow domain, and 550045_30, which shows a VB zone (seen as a CTRZ) in the chamber downstream of the dump plane. The plots of V_t and V_z vs radial position, symmetrized Q vs radial position, and symmetrized K vs Q are shown next. The L and R subscripts in the plot legends refer to the left and right sides, respectively. These subscripts are included in the legend because, as described previously, the data are divided along the centerline for each configuration.

Figure 10 shows the 3-D contour of axial velocity for the swirler n303030_30. The figure shows V_z peaking around the exit of the

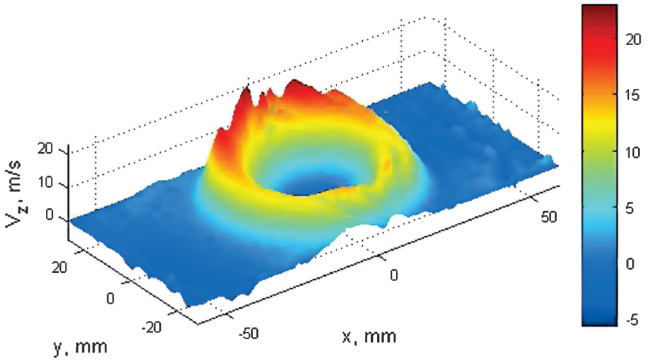

Fig. 10 3-D plot of axial velocity on the imaged plane for n303030_30.

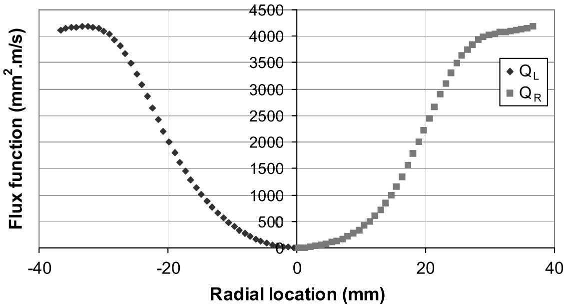

Fig. 11 Flux function for n303030_30.

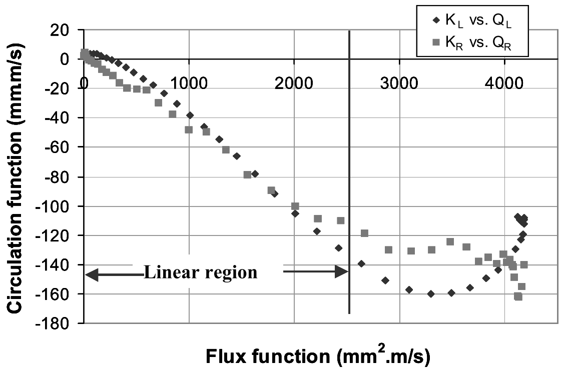

Fig. 12 Plot of circulation vs flux function showing linear region for n303030_30.

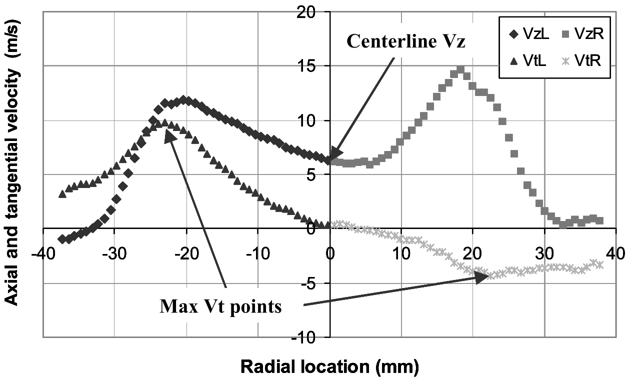

Fig. 13 Plot of axial velocity and tangential velocity vs radial location for n303030_30.

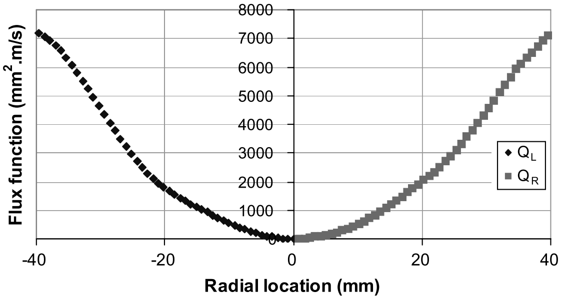

Fig. 15 Flux function for 500045_30.

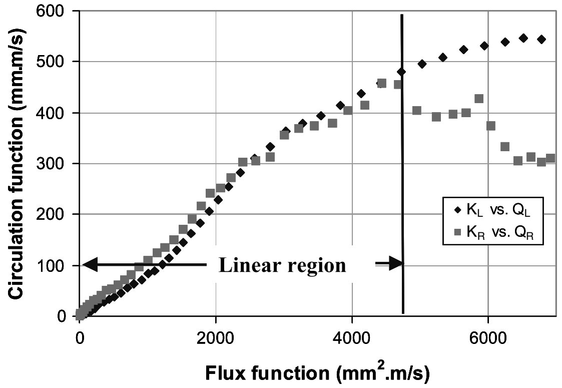

Fig. 16 Plot of circulation vs flux function showing linear region for 550045_30.

mixing tube, very low velocity in the center, and low to negative velocity toward the walls of the chamber. There is also axisymmetry in the observed flow, most likely due to the nature of the vortex flow. For our analysis, we are concerned primarily with the area of the flow that is influenced by the swirler. For most of the configurations tested, this corresponds to the range $-40\ \text{mm} \leq r \leq 40\ \text{mm}$. The region outside this range is dominated by the CRZs, which are generated by the viscous effect with chamber walls and result in small, negative axial speed. Therefore, this range is not included in our calculations of Q, K, ω, and Ω. Also note that on the y axis, we are limited to $-28\ \text{mm} \leq y \leq 28\ \text{mm}$ by the camera viewing area.

Figure 11 shows the computed flux function Q after it has been symmetrized to compensate for a slight offset of the flow center from the $r = 0$ point due to PIV calibration. The plot of circulation vs flux function in Fig. 12 shows that the line for the left side is laying close to the line for the right side, and both are nearly linear, demonstrating that the assumption of solid-body rotation at the swirler exit plane is relevant. To calculate Ω for this configuration, we take the average of the slopes of K_L vs Q_L and K_R vs Q_R in the linear region shown in Fig. 12. From this, we find $\Omega = 0.63 \pm 0.03$ (or $S_N = 0.32 \pm 0.02$) for the configuration with swirler n303030_30. To calculate ω, we use Fig. 13 to determine $Vt_{\max}$ at the left and right sides, average between them, and obtain

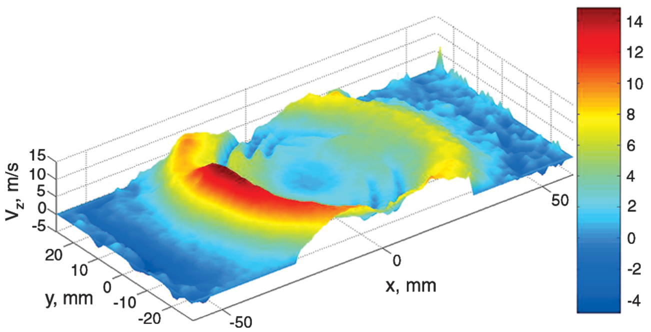

Fig. 14 3-D plot of axial velocity on the imaged plane for 500045_30.

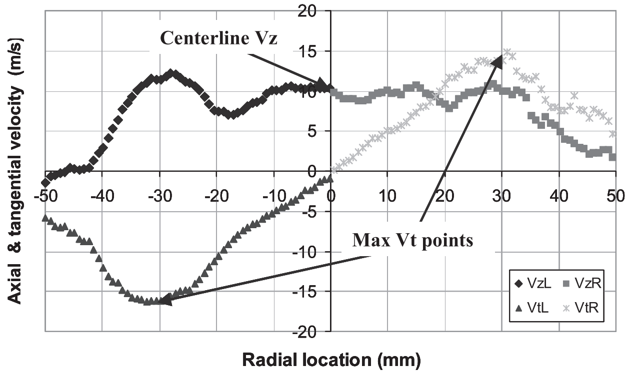

Fig. 17 Plot of axial velocity and tangential velocity vs radial location for 550045_30.

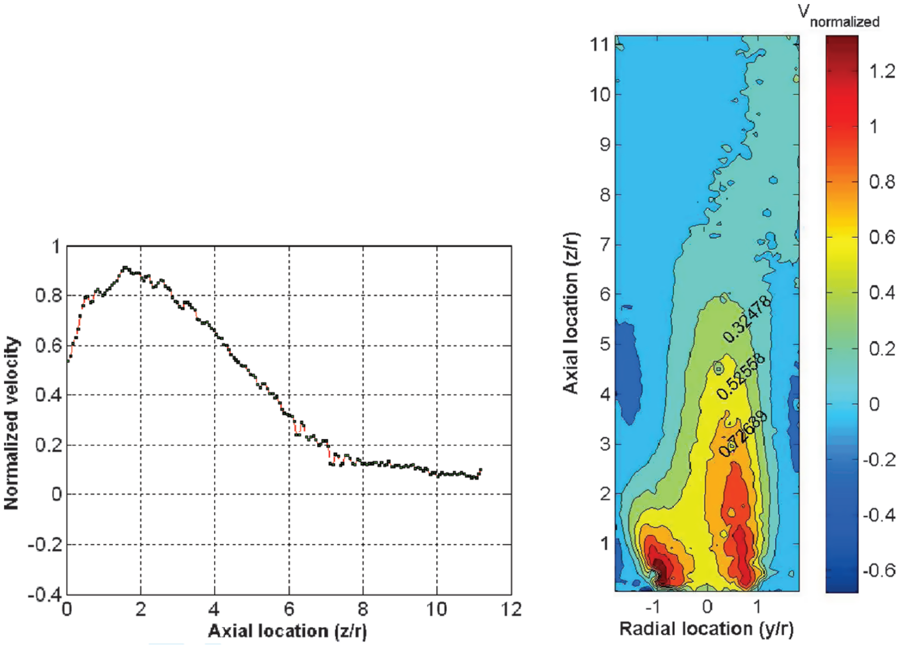

Fig. 18 Normalized axial velocity along the chamber centerline and normalized axial velocity contour along the chamber centerline plane for n303030_30.

$$\omega = (V_{t_L} + V_{t_R})/(2V_{z0}) = 0.53 \pm 0.04$$

for the configuration with swirler n303030_30. Note that, for the configuration with swirler n303030_30, both swirl ratios are less than the predicted critical values, $\Omega = 0.63 < 0.88$ and $\omega = 0.53 \leq 0.75$; therefore, it is expected that VB does not appear inside the flow domain for this configuration.

The plots for analyzing 550045_30 are shown in Figs. 14–17 and yield $\Omega = 1.31 \pm 0.04$ (or $S_N = 0.66 \pm 0.02$) and $\omega = 1.45 \pm 0.04$. Note that, for this configuration, the swirl ratios are higher than for the previous configuration. Both swirl ratios are greater than the predicted critical values; that is, $\Omega = 1.31 > 1$ as well as $\Omega = 1.31 < 1.87$ and $\omega = 1.45 > 0.75$. Therefore, it is expected here that VB appears inside the flow domain downstream of dump plane.

As earlier stated, the 2-D PIV data for each configuration yield the axial location of VB for that swirler combination. A plot of normalized axial velocity along the centerline plane versus normalized axial location and a contour plot of the same parameters are made for each swirler. The former plot provides the axial location for breakdown along the centerline of the chamber, while the latter gives a global, quantitative view of the flow structure. Figure 18 shows, as predicted previously, that there is no VB with swirler n303030_30, since normalized velocity does not go below zero at any point along the axis. On the other hand, Fig. 19 shows, again as predicted previously, that a long and wide VB zone occurs at these flow conditions; it starts at $x_{\mathrm{BD}}/R = 0.37 \pm 0.02$ for the configuration with swirler 550045_30 and extends far downstream until $x/R \approx 8$, and even beyond with a narrower near-stagnant flow zone.

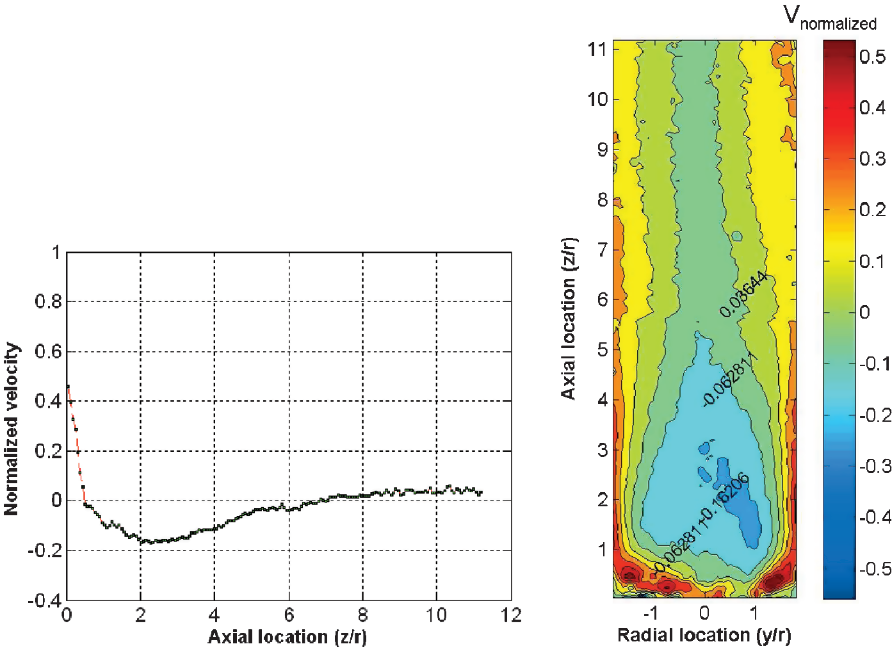

Fig. 19 Normalized axial velocity along the chamber centerline and normalized axial velocity contour along the chamber centerline plane for 550045_30.

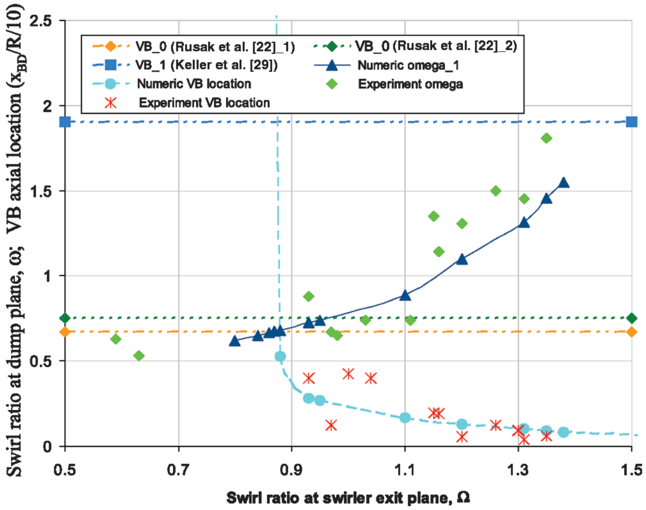

Fig. 20 Swirl ratio at dump plane ω and normalized axial VB location vs swirl ratio at swirler exit plane Ω for computational and experiment results.

IV. Discussion of Results

The results of data analysis from experiments with 2-D and 3-D PIV velocity measurements for a wide set of swirlers and a domain with an expansion ratio of approximately 2.5 are summarized in Fig. 20. The figure is built on the earlier plot in Fig. 6. The experimentally computed points are added to this figure. The red stars are the experimental points of the breakdown position [$(x_{\mathrm{BD}}/R)/10$ vs the swirl number Ω at the swirler exit plane]. The bright green diamonds are the experimentally computed points of swirl ratio ω at the dump plane vs the swirl number Ω at the swirler exit plane. The figure also includes the theoretically predicted critical swirl ratio at the dump plane for the experimental apparatus, i.e., the horizontal green dotted line at $\omega = 0.75$. This is identified with subscript 2 in the legend. Subscript 1 in the legend for the horizontal orange dotted line, on the other hand, refers to the theoretically predicted critical swirl ratio at the dump plane for the numerical computations shown in Fig. 6. Table 2 summarizes the experimental data points. In this table, the typical accuracy of results for Ω is ± 0.03, and it is ± 0.04 for ω and ± 0.02 for x_{BD}/R. It can be seen that, as expected, all the 2-D PIV data taken for configurations with calculated swirl ratio at the dump plane $\omega < 0.75 \pm 0.02$ (i.e.. experimental data points below the green dotted line) show no VB in the entire domain. Figure 18 shows an example of such a flowfield for the configuration with swirler n303030_30. Figure 20 also shows that when $\omega > 0.75$, a VB state appears in the chamber, and this is verified in Fig. 20. The critical swirl number for the first appearance of breakdown in the dump region of the experimental apparatus is $\Omega \approx 1.03 \pm 0.03$. Figure 20 shows that the trend for the numerical results and the experimental results are very similar for both x_{BD}/R vs Ω and ω vs Ω. The scatter observed in the experimental data in Fig. 20 results from flow unsteadiness that occurs as breakdown appears in the domain and from PIV-measurement noise that may also be attributed to the unsteady nature of such flows.

Table 2 Summary of experimental data in Fig. 20

	Configuration	Ω	ω	$VB/r/10$	Wa (g/s)	Re
1	n304545	0.59	0.63	n/a	30.0	40,865
2	n303030	0.63	0.53	n/a	30.1	41,001
3	n454545	0.93	0.88	0.400	30.0	40,865
4	n300045	0.97	0.67	0.122	29.9	40,729
5	300045	0.98	0.65	n/a	30.0	40,865
6	300045	1.03	0.74	n/a	30.1	41,001
7	300045	1.11	0.74	n/a	50.0	67,000
8	n550045	1.15	1.35	0.194	30.0	40,865
9	n450045	1.16	1.14	0.190	30.0	40,865
10	n554545	1.20	1.31	0.056	30.0	40,865
11	450045	1.26	1.50	0.123	48.9	66,610
12	550045	1.31	1.45	0.037	30.3	41,273
13	450045	1.35	1.81	0.058	30.0	40,865

It is also observed that an increase in airflow rate for the same swirler configuration results in a decrease in swirl ratios Ω and ω and a delay in breakdown; that is, the axial VB location is pushed farther away from the dump plane. This can be explained by the increase in both the Reynolds number and Mach number of the flow, which both act to delay the onset of breakdown.

V. Conclusions

The appearance of VB states in inert flows in finite length chambers relevant to premixed combustor configurations can be predicted by theoretical tools and simulated by numerical means. The theoretical predictions show good agreement with experimental data from PIV measurements. In addition, the experiments support the validity of the theoretical and numerical tools.

The ultimate benefit of understanding the VB characteristics in relation to the swirling fuel injector and the flow variables affecting the flow profile is the ability to actively vary the inlet swirl ratio of a LPM swirl-stabilized combustor without inducing either flame blowout or flashback based on knowledge of global conditions. Furthermore, this knowledge may also be employed to design fuel injectors, which provide optimum fuel–air mixing without introducing potentially damaging phenomena such as combustion pressure dynamics, which is also referred to as combustion dynamics. The appearance and location of VB states can be predicted with reasonable accuracy from knowledge of swirl ratio and global flow conditions. The next step in this work is to investigate the VB trends under premixed combustion and possibly relate the observations to other phenomena observed in LPM combustor systems, such as combustion dynamics, emissions, lean blowout, and fuel nozzle burn.

References

[1] Correa, S. M., "A Review of NOx Formation Under Gas-Turbine Combustion Conditions," *Combustion Science and Technology*, Vol. 87, No. 1, 1993, pp. 329–362.
doi:10.1080/00102209208947221

[2] Turns, S. R., *An Introduction to Combustion: Concepts and Applications*, 2nd ed., McGraw–Hill, Boston, 2000.

[3] Huang, Y., Sung, H., Hsieh, S., and Yang, V., "Large-Eddy Simulation of Combustion Dynamics of Lean-Premixed Swirl-Stabilized Combustor," *Journal of Propulsion and Power*, Vol. 19, No. 5, Sept.–Oct. 2003, pp. 782–794.
doi:10.2514/2.6194

[4] Paschereit, C. O., and Gutmark, E., "Proportional Control of Combustion Instabilities in a Simulated Gas-Turbine Combustor," *Journal of Propulsion and Power*, Vol. 18, No. 6, Nov.–Dec. 2002, pp. 1298–1304.
doi:10.2514/2.6067

[5] Syred, N., and Beér, J. M., "Combustion in Swirling Flow: A Review," *Combustion and Flame*, Vol. 23, No. 2, 1974, pp. 143–201.
doi:10.1016/0010-2180(74)90057-1

[6] McManus, K. R., Poinsot, T., and Candel, S. M., "A Review of Active Control of Combustion Instabilities," *Progress in Energy and Combustion Science*, Vol. 19, No. 1, 1993, pp. 1–29.
doi:10.1016/0360-1285(93)90020-F

[7] Grinstein, F. F., Young, T. R., Gutmark, E. J., Li, G., Hsiao, G., and Mongia, H. C., "Flow Dynamics in a Swirl Combustor," *Journal of Turbulence*, Vol. 3, No. 1, 2002, p. 30.
doi:10.1088/1468-5248/3/1/030

[8] Konle, M., Kiesewetter, F., and Sattelmayer, T., "Simultaneous High Repetition Rate PIV-LIF Measurements of CIVB Driven Flashback," *Experiments in Fluids*, Vol. 44, No. 4, 2008, pp. 529–538.
doi:10.1007/s00348-007-0411-2

[9] Wang, S., and Rusak, Z., "The Dynamics of a Swirling Flow in a Pipe and Transition to Axisymmetric Vortex Breakdown," *Journal of Fluid Mechanics*, Vol. 340, 1997, pp. 177–223.
doi:10.1017/S0022112097005272

[10] Hall, M. G., "Vortex Breakdown," *Annual Review of Fluid Mechanics*, Vol. 4, 1972, pp. 195–218.
doi:10.1146/annurev.fl.04.010172.001211

[11] Leibovich, S., "The Structure of Vortex Breakdown," *Annual Review of Fluid Mechanics*, Vol. 10, 1978, pp. 221–246. doi:10.1146/annurev.fl.10.010178.001253

[12] Leibovich, S., "Vortex Stability and Breakdown: Survey and Extension," *AIAA Journal*, Vol. 22, No. 9, 1984, pp 1192–1206. doi:10.2514/3.8761

[13] Escudier, M., "Vortex Breakdown: Observations and Explanations," *Progress in Aerospace Sciences*, Vol. 25, No. 2, 1988, pp. 189–229. doi:10.1016/0376-0421(88)90007-3

[14] Sarpkaya, T., "Vortex Breakdown and Turbulence," *33rd Aerospace Sciences Meeting and Exhibit*, AIAA Paper 1995-0433, 1995.

[15] Althaus, W., Bruecker, C., and Weimer, M., "Breakdown of Slender Vortices," *Fluid Vortices*, edited by S. I. Green, Kluwer Academic, Norwell, MA, 1995, pp. 373–426.

[16] Rusak, Z., and Wang, S., "Review of Theoretical Approaches to The Vortex Breakdown Phenomenon," *1st Theoretical Fluid Mechanics Meeting*, AIAA Paper 1996-2126, 1996.

[17] Wang, S., and Rusak, Z., "On the Stability of an Axisymmertic Rotating Flow in a Pipe," *Physics of Fluids*, Vol. 8, No. 4, April 1996, pp. 1007–1016.
doi:10.1063/1.868882

[18] Wang, S., and Rusak, Z., "On the Stability of Non-Columnar Swirling Flows," *Physics of Fluids*, Vol. 8, No. 4, 1996, pp. 1017–1023. doi:10.1063/1.868878

[19] Wang, S., and Rusak, Z., "The Effect of Slight Viscosity on a Near-Critical Swirling Flow in a Pipe," *Physics of Fluids*, Vol. 9, No. 7, 1997, pp. 1914–1927.
doi:10.1063/1.869312

[20] Malkiel, E., Cohen, J., Rusak, Z., and Wang, S., "Axisymmetric Vortex Breakdown in a Pipe: Theoretical and Experimental Studies," *Proceedings of the 36th Israel Annual Conference on Aerospace Sciences*, Omanuth Press, Haifa, Israel, 1996, pp. 24–34.

[21] Rusak, Z., Whiting, C. H., and Wang, S., "Axisymmetric Breakdown of a *Q*-Vortex in a Pipe," *AIAA Journal*, Vol. 36, No. 10, Oct. 1998, pp. 1848–1853.
doi:10.2514/2.277

[22] Rusak, Z., Wang, S., and Whiting, C. H., "The Evolution of a Perturbed Vortex in a Pipe to Axisymmetric Vortex Breakdown," *Journal of Fluid Mechanics*, Vol. 366, 1998, pp. 211–237.
doi:10.1017/S0022112098001396

[23] Judd, K., Rusak, Z., and Hirsa, A., "Theoretical and Experimental Studies of Swirling Flows in Diverging Streamtubes," *Advances in Fluid Mechanics III*, edited by M. Rahman and C. A. Brebbia, WIT Press, Bilerica, MA, 2000, pp. 491–502.

[24] Rusak, Z., "Review of Recent Studies on the Axisymmetric Vortex Breakdown Phenomenon," *Fluids 2000 Conference and Exhibit*, AIAA Paper 2000-2529, 2000.

[25] Rusak, Z., and Lee, J. H., "The Effect of Compressibility on the Critical Swirl of Vortex Flows in a Pipe," *Journal of Fluid Mechanics*, Vol. 461, 2002, pp. 301–319.
doi:10.1017/S0022112002008431

[26] Umeh, C. O., and Rusak, Z., "Swirling Flows And Vortex Breakdown in an Axisymmetric Lean Premixed Combustor," *36th AIAA Fluid Dynamics Conference and Exhibit*, AIAA Paper 2006-3732, 2006.

[27] Fluent 5 User's Guide, Vol. 1, Fluent, Inc., Ann Arbor, MI, 1998.

[28] Umeh, C. O., "Stability of Swirling Flows in an Axisymmetric Lean Premixed Combustor," M.S. Thesis, Rensselaer Polytechnic Inst., Troy, NY, 2005.

[29] Keller, J. J., Egli, W., and Exley, J., "Force-and Loss-Free Transitions Between Vortex Flow States," *Studies of Vortex Dominated Flows, Proceedings of the Symposium on Vortex Dominated Flows*, Springer–Verlag, New York, July 1985, pp. 63–75.

[30] Li, G., and Gutmark, E. J., "Boundary Condition Effects on Nonreacting and Reacting Flows in a Multiswirl Combustor," *AIAA Journal*, Vol. 44, No. 3, March 2006, pp. 444–456.
doi:10.2514/1.15675

T. Jackson
Associate Editor